Technical Note

Flow in Porous Metallic Materials: A Magnetic Resonance Imaging Study

Shoujun Xu, PhD,[1,2] Elad Harel, PhD,[1,2] David J. Michalak, PhD,[1,2] Charles W. Crawford, MSc,[1,2] Dmitry Budker, PhD,[3,4]* and Alexander Pines, PhD[1,2]

Purpose: To visualize flow dynamics of analytes inside porous metallic materials with laser-detected magnetic resonance imaging (MRI).

Materials and Methods: We examine the flow of nuclear-polarized water in a porous stainless steel cylinder. Laser-detected MRI utilizes a sensitive optical atomic magnetometer as the detector. Imaging was performed in a remote-detection mode: the encoding was conducted in the Earth's magnetic field, and detection is conducted downstream of the encoding location. Conventional MRI (7T) was also performed for comparison.

Results: Laser-detected MRI clearly showed MR images of water flowing through the sample, whereas conventional MRI provided no image.

Conclusion: We demonstrated the viability of laser-detected MRI at low-field for studying porous metallic materials, extending MRI techniques to a new group of systems that is normally not accessible to conventional MRI.

Key Words: low-field MRI; laser detection, porous metal; flow imaging; remote detection; penetration depth
J. Magn. Reson. Imaging 2008;28:1299–1302.

MAGNETIC RESONANCE IMAGING (MRI), conventionally performed in a strong homogenous magnetic field, is a versatile imaging modality for materials research (1). Its advantage of noninvasiveness allows imaging of opaque porous materials not possible by optical methods. Sederman et al (2) used MRI to study the structure-flow correlation in packed beds. Seymour et al (3) studied biofouling of a homogeneous model porous media. Callaghan and Khrapitchev (4), and Blümich et al (5) developed various pulse sequences to investigate time-dependent flow velocities in porous media. Swider et al (6) employed high-resolution MRI to study both localized and global flow in porous biomaterials. Recently, Granwehr et al (7) developed a time-of-flight MRI scheme that utilized remote detection to study the flow behavior of xenon gas in porous rocks. In addition, different fluids can be selectively encoded based on their respective chemical shifts (8). The samples involved in these studies with conventional MRI are limited to electrically nonconductive materials.

Flow dynamics of liquids in porous metallic materials is of extensive practical interest, as these materials are widely used in filtration, catalysis, and biomedicine (9–12). Conventional MRI techniques, however, are not applicable to these materials for two fundamental reasons. First, the penetration depth of radiofrequency radiation, which is inversely proportional to the square root of the frequency, is only several micrometers in metals for the strong magnetic fields (>1 T) used in conventional MRI scanners (13). The nuclear spins within an electrically conductive sample that reside deeper than the penetration depth will not be sufficiently excited, and thus, will not contribute to the MR images. Even if some nuclear spins could be excited within a region sufficiently below the penetration depth of the metallic sample, these spins would not be detected at the pickup coil, because their oscillating field would be similarly screened out. Second, the large magnetic-susceptibility gradients intrinsically associated with porous metallic materials significantly distort the field homogeneity at high-field, imposing an overwhelming distortion on MR images (14).

To overcome the difficulties mentioned above, one viable solution is to perform MRI in ultra-low magnetic fields (15) on the order of several microtesla (μT). In such low magnetic fields, the Larmor precession frequency is much lower (in the audiofrequency range) and, as a consequence, it has a much larger penetration depth through metallic materials. In addition, the distortion of the encoding field caused by magnetic sus-

[1]Materials Sciences Division, Lawrence Berkeley National Laboratory, University of California, Berkeley, California, USA.
[2]Department of Chemistry, University of California, and Nuclear Sciences Division, Lawrence Berkeley National Laboratory, Berkeley, California, USA.
[3]Department of Physics, University of California, Berkley, California, USA.
[4]Nuclear Sciences Division, Lawrence Berkley National Laboratory, Berkley, California, USA.
Contract grant sponsor: Office of Naval Research (ONR) Multidisciplinary University Research Initiative (MURI); Contract grant sponsor: Nuclear Sciences Division, U.S. Department of Energy; Contract grant sponsor: Director, Office of Science, Office of Basic Sciences, Materials Sciences Division, U.S. Department of Energy; Contract grant number: DE-AC03-76SF00098.
*Address reprint requests to: D.B., Room 273, Birge Hall, University of California, Berkeley, CA 94720. E-mail: budker@berkeley.edu
Received February 4, 2008; Accepted July 8, 2008.
DOI 10.1002/jmri.21532
Published online in Wiley InterScience (www.interscience.wiley.com).

ceptibility differences also becomes insignificant in an ultra-low field, and the resulting images only suffer negligible distortion.

Alternative detection techniques must be implemented for ultra-low-field MRI because conventional Faraday detection has poor sensitivity in low magnetic fields (16). Superconducting quantum interference devices (SQUIDs) provide a sensitivity that is independent of the field strength (17), and this technique has successfully imaged objects within a metallic enclosure and has produced undistorted images in the presence of a titanium bar (14). No direct study on porous metallic materials has, however, been reported. Here, we present MRI studies on a porous metallic material, rather than the effect of a metal object in the vicinity of a nonconductive sample. We use an optical atomic magnetometer as the detector, which has a better sensitivity than a Faraday coil at ultra-low-field and requires no cryogenics, in contrast to SQUIDs. The encoding is conducted in the Earth's magnetic field (~40 μT). For comparison, we performed high-field time-resolved images of water flowing through the same porous stainless-steel material.

MATERIALS AND METHODS

The instrument used in this work has been described previously by Xu et al (18). Briefly, it is a first-order gradiometer containing two atomic magnetometers. A linearly polarized laser beam is frequency-modulated to generate magneto-optical resonance. The wavelength of the light is 794 nm, matching the D1 transition of ^{87}Rb. Fluids to be measured are introduced in the vicinity of the detectors within a leading-field solenoid. The detectors are located outside the solenoid and are insensitive to the leading field, while they are sensitive to the fields produced by the sample. The differential-field sensitivity of the gradiometer is ~ 80 fT/(Hz)$^{1/2}$ for near-DC detection. For comparison purposes, a high-field measurement is performed with a commercial 7T spectrometer (proton precession frequency 300 MHz).

The sample under study is a porous stainless-steel cylinder 9.5 mm in diameter and 12.5 mm in length (Applied Porous Technologies). The average pore size is <1 mm. The porosity, which is defined as the ratio between the total volume of the pores and the volume of the sample cylinder, is measured to be ~60%. The sample was held in a Teflon holder that allowed for running the experiment with or without the sample.

The experimental schematic is shown in Fig. 1. Water is prepolarized in the 0.6T magnetic field of a permanent magnet, indicated in Fig. 1a. High-pressure nitrogen gas is used to drive the water; the pressure of nitrogen is adjusted so water reaches the detectors at approximately the same time with and without the steel sample. Water flows through the sample (or the empty Teflon holder) where the spatial encoding takes place (Fig. 1b). The direction of the Earth's magnetic field, B_E, is indicated by the arrow. A coil wrapped around the sample holder is for spin inversion and spatial encoding. A π pulse is shown for the case of spin inversion. In order to obtain flow images of water inside the sample, we use a phase-encoding pulse sequence that has been

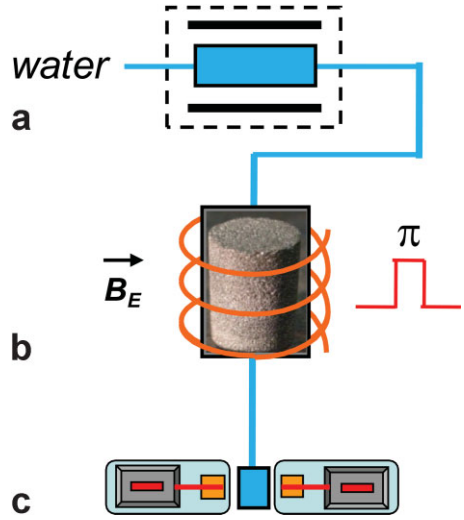

Figure 1. A schematic of Earth-field, laser-detected MRI of water flow. It consists of (**a**) prepolarization of the protons of water by a 0.6T magnetic field (black bars represent permanent magnets, which are housed in a magnetic shield indicated by the dash-lined box), (**b**) spatial encoding within the porous stainless-steel sample in the Earth's magnetic field in our laboratory (40 μT, along the direction of the arrow), and (**c**) detection with a gradiometer formed by two atomic magnetometers. Water is indicated in blue. [Color figure can be viewed in the online issue, which is available at www.interscience.wiley.com.]

described previously by Granwehr et al (7) and Xu et al (19). Briefly, a π/2 pulse is applied to excite the nuclear spins into the transverse plane; the spins precess for a fixed time in the presence of gradient magnet fields (0.2 μT/mm along the flow dimension, and 0.1 μT/mm perpendicular to the flow); the gradients are turned off and the spins are tipped back into the longitudinal axis by a second π/2 pulse. Finally the spatially-encoded water proceeds to flow into the detection region for measurement (Fig. 1c).

RESULTS

We first measured the overall signal from the water in the sample using both the conventional high-field instrument and at the Earth's field using the laser atomic magnetometer. No signal is detected by the 7T nuclear MR (NMR) spectrometer when the sample is present, due to the screening of the radiofrequencies by the metallic sample. For the low-field measurements, the nuclear spins in the sample are inverted by a π pulse (1.7 kHz, 2-msec duration). Flow spectra as a function of the arrival time are obtained based on the transient magnetization of the water as it flows past the atomic magnetometers (Fig. 2). The arrival time is the time interval between the end of the π pulse and the arrival of water at the magnetometers. From the two traces in Fig. 2, one without the sample (red) and one with the sample (blue), we see that adding the stainless-steel sample only decreases the signal by a percentage (~40%), in contrast to what occurs at high-field. This decrease is mainly caused by the volume change and

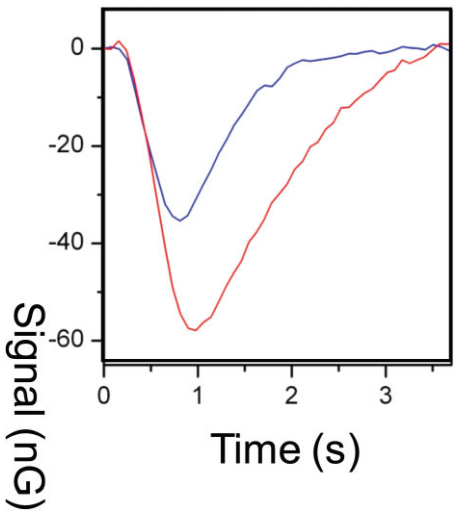

Figure 2. NMR signal from the water occupying the measurement volume measured with the atomic gradiometer. The time axis is the arrival of water at the detection region, with time zero referenced as the end of the inversion pulse. Red trace: signal when the porous sample is not in the measuring volume; blue trace: signal with the porous sample present. [Color figure can be viewed in the online issue, which is available at www.interscience.wiley.com.]

the enhanced relaxation of water due to the presence of the sample. (The arrival times corresponding to the maximum signal in the two flow spectra are a little different due to slightly different flow conditions.) These results demonstrate that the imaging problems encountered at high-field can be significantly overcome at low-field.

The flow images measured by the magnetometers are demonstrated in Fig. 3a. The images were obtained from a series of flow spectra in which the gradient fields are varied according to the phase encoding pulse sequence described in the experimental section. The images are presented as a function of the arrival time of the water. For comparison, the results obtained from the conventional NMR spectrometer are shown in Fig. 3b, where no images in the sample region are observed. (The only available signal in those images comes from the junction regions before and after the porous metallic sample.)

DISCUSSION

From the flow spectra, we see that the spin-inverted water in the sample region first arrives at the detection region after 0.4 seconds, the signal peaks after 0.8 seconds, and then gradually decreases due to the water flowing out of the detection region and simultaneously undergoing longitudinal relaxation. It also shows that the water signal reaches maximum faster than the time it takes for the water to completely flow out of the detection region. The overall flow resistance is dominated by the porous sample, as evidenced by the much higher pressure of nitrogen required to drive the water through the sample at the same flow rate, compared to when the sample is absent.

The images as a function of arrival time reveal the spatial information on the water that is detected. At 0.4 seconds after spatial encoding, only the downstream water, closest to the detectors, reaches the detection region. This can be seen in the two-dimensional (2D) image at 0.4 seconds, and it corresponds to the starting point of the flow spectra (blue trace). By 0.8 seconds, almost all the water in the steel sample has arrived at the detectors; the encoded water of Fig. 3a at 0.8 seconds covers the entire sample region. This is consistent with the flow spectrum (blue trace) in Fig. 2, where the

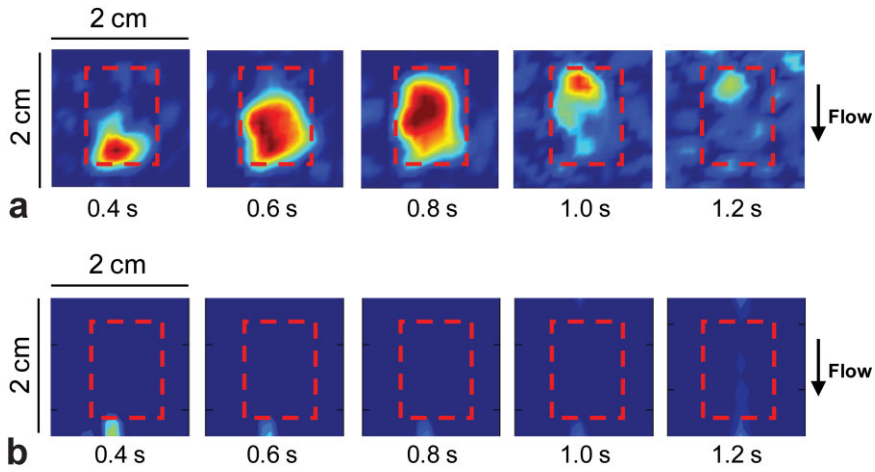

Figure 3. Flow images obtained with a time-of-flight imaging sequence: (**a**) detected by the atomic magnetometers; (**b**) detected by the 7T NMR spectrometer. The red rectangle indicates the location of the sample area. The time underneath each image represents the corresponding arrival time of the encoded water after the end of the second $\pi/2$ pulse. False color is used to indicate the relative intensity of the images: dark blue for background and red for the most intense spin density. Some background noise exists outside of the sample region in low-field images. The magnetometer-detected images are reconstructed from the averaged data of 30 repeated phase-encoding cycles. The overall duration for obtaining these images is six hours, which is governed by the signal-to-noise ratio of the magnetometers and the flow time of water under current condition. [Color figure can be viewed in the online issue, which is available at www.interscience.wiley.com.]

maximum signal occurs at 0.8 second. The 2D flow image at 1.2 seconds shows that the upstream water, farthest from the detectors, flows into the detection region last. At times later than 1.2 seconds, the flow images become noisy and the signal from water eventually disappears. This again corresponds to the decrease of signal in the flow spectrum (blue trace) in Fig. 2. The spatial resolution of the images is 1.5 mm along the flow direction and 1.5 mm perpendicular to the flow.

Our low-field flow images show that the central region of the images has a higher proton density. Qualitatively, this is because the sample is of cylindrical geometry and the 2D images are the line integral of the proton density along the third spatial dimension. We also do not observe abrupt intensity change in the images. Hence, these images demonstrate that, within our (~1.5-mm) resolution, the porosity of the stainless-steel cylinder is homogeneous throughout the entire interior volume; this corroborates the known microporous structure provided to us by the supplier. The inlet and outlet regions are not seen here because they have much less volume than the sample region.

We compare this study in which the encoding takes place in the Earth's magnetic field with a previous study performed at 3 mT (19). The 3-mT magnetic field was provided by a giant solenoid running at 5-Å current, with a homogeneity of ~1000 ppm in the field-of-view. The gradient magnetic fields are on the order of 2 μT/mm. In contrast, the Earth's magnetic field is ubiquitous and homogeneous, and no power supply is required to generate a magnetic field. The gradients in this work are one order of magnitude lower than the previous work, and the powerful current amplifiers are no longer required. As a result, Earth-field MRI is more portable and less power-consuming. Imaging in the Earth's field also enables the study of very large samples. This contrasts with MRI in a finite magnetic field generated by electric currents or permanent magnets, where there are tremendous technical difficulties associated with generating a strong and homogeneous magnetic field across the field of view of a large sample.

In conclusion, our laser-detected MRI technique clearly demonstrates the capability of studying flow phenomena in opaque materials with large differences in the magnetic-susceptibility, which is prohibitively difficult with other techniques. With further optimization in sensitivity and configuration (20–22), a portable MRI scanner based on optical atomic magnetometry could be available for revealing quantitative flow information in a wide range of materials that are excluded from conventional MRI study.

ACKNOWLEDGMENT

Supported in part by grants from the Office of Naval Research (ONR) Multidisciplinary University Research Initiative (MURI) and the Nuclear Sciences Division of the U.S. Department of Energy (both to D.B).

REFERENCES

1. Blümich B. NMR imaging of materials. Oxford: Oxford University Press; 2000. 568 p.
2. Sederman AJ, Johns ML, Alexander P, Gladden LF. Structure-flow correlations in packed beds. Chem Eng Sci 1998;53:2117–2128.
3. Seymour JD, Gage JP, Codd SL, Gerlach R. Magnetic resonance microscopy of biofouling induced scale dependent transport in porous media. Adv Water Resour 2007;30:1408–1420.
4. Callaghan PT, Khrapitchev AA. Time-dependent velocities in porous media dispersive flow. Magn Reson Imaging 2001;19:301–305.
5. Blümich B, Callaghan PT, Damion RA, et al. Two-dimensional NMR of velocity exchange: VEXSY and SERPENT. J Magn Reson 2001; 152:162–167.
6. Swider P, Conroy M, Pedrono A, et al. Use of high-resolution MRI for investigation of fluid flow and global permeability in a material with interconnected porosity. J Biomechanics 2007;40:2112–2118.
7. Granwehr J, Harel E, Han SI, Garcia S, Pines A. Time-of-flight flow imaging using NMR remote detection. Phys Rev Lett 2005;95:075503.
8. Harel E, Granwehr J, Seeley J, Pines A. Multiphase imaging of gas flow in a nanoporous material using remote detection NMR. Nat Mater 2006;5:321–327.
9. Nakajima H. Fabrication, properties and application of porous metals with directional pores. Prog Mater Sci 2007;52:1091–1173.
10. Banhart J. Manufacture, characterization and application of cellular metals and metal foams. Prog Mater Sci 2001;46:559-U3.
11. Cognet P, Berlan J, Lacoste G, Fabre PL, Jud JM. Application of metallic foams in an electrochemical pulsed flow reactor. 2. Oxidation of benzyl alcohol. J Appl Electrochem 1996;26:631–637.
12. Ryan G, Pandit A, Apatsidis DP. Fabrication methods of porous metals for use in orthopedic applications. Biomaterials 2006;27: 2651–2670.
13. Bennett CR, Wang PS, Donahue MJ. Artifacts in magnetic resonance imaging from metals. J Appl Physiol 1996;79:4712–4714.
14. Mößle M, Han SI, Myers WR, et al. SQUID-detected microtesla MRI in the presence of metal. J Magn Reson 2006;179:146–151.
15. Mohorič A, Planinšič G, Kos M, Duh A, Stepišnik J. Magnetic resonance imaging system based on Earth's magnetic field. Instru Sci Technol 2004;32:655–667.
16. Halse ME, Coy A, Dykstra R, et al. A practical and flexible implementation of 3D MRI in the Earth's magnetic field. J Magn Reson 2006;182:75–83.
17. Kleiner R, Koelle D, Ludwig F, Clarke J. Superconducting quantum interference devices: state of the art and applications. Proc IEEE 2004;92:1534–1548.
18. Xu SJ, Rochester SM, Yashchuk VV, Donaldson MH, Budker D. Construction and applications of an atomic magnetic gradiometer based on nonlinear magneto-optical rotation. Rev Sci Instrum 2006;77:083106.
19. Xu SJ, Yashchuk VV, Donaldson MH, Rochester SM, Budker D, Pines A. Magnetic resonance imaging with an optical atomic magnetometer. Proc Natl Acad Sci USA 2006;103:12668–12671.
20. Kominis IK, Kornack TW, Allred JC, Romalis MV. A subfemtotesla multichannel atomic magnetometer. Nature 2003;422:596–599.
21. Budker, D, Romalis, MV. Optical magnetometry. Nat Phys 2007;3: 227–304.
22. Schwindt PDD, Lindseth B, Knappe S, Shah V, Kitching J, Liew LA. Chip-scale atomic magnetometer with improved sensitivity by use of the M_x technique. Appl Phys Lett 2007;90:081102.